PNAS RESEARCH ARTICLE | PHYSICS

Hierarchy of topological transitions in a network liquid

Andreas Neophytou[a,b,1], Francis W. Starr[c], Dwaipayan Chakrabarti[b,d], and Francesco Sciortino[a,1]

Edited by Erio Tosatti, Scuola Internazionale Superiore di Studi Avanzati, Trieste, Italy; received April 5, 2024; accepted June 30, 2024

The representation of complex systems as networks has become a critical tool across many fields of science. In the context of physical networks, such as biological neural networks, vascular networks, or network liquids where the nodes and edges occupy volume in three-dimensional space, the question of how they become densely packed is of special importance. Here, we investigate a model network liquid, which is known to densify via two successive liquid–liquid phase transitions (LLPTs). We elucidate the importance of rings—cyclic paths formed by bonded particles in the networks—and their spatial disposition in understanding the structural changes that underpin the increase in density across the LLPTs. Our analyses demonstrate that the densification of these networks is primarily driven by the formation of linked rings, and the LLPTs correspond to a hierarchy of topological transitions where rings form the fundamental building blocks. We envisage entanglement to emerge as a general mechanism for densification, with wide implications for the embedding of physical networks, especially in confined spaces.

Significance

Understanding the fundamental principles which govern the structure and layout of physical networks—networks composed of nodes and edges that occupy space and cannot overlap with each other—has recently emerged as an important open question. As a test case, we investigate the densification of physical networks formed by DNA-functionalized nanoparticles. These particles have the capability to self-assemble into three distinct networks with notably different densities, each separated by first-order phase transitions. We reveal that these phase transitions signify a series of hierarchical transitions driven by the topological linking of rings, which is the key to producing physical networks satisfying excluded volume constraints.

networks | topology | DNA nanotechnology | liquid–liquid phase transition | self-assembly

Networks—collections of nodes connected by edges—have become central to modern life, they control the flow of power, transportation, and even our social interactions (1). All the information required to describe a network is contained in its adjacency matrix ($\mathcal{A}$): a square symmetric matrix with rows and columns whose indices represent a node and a 1 or 0 in position $\mathcal{A}_{ij}$ according to whether nodes i and j are connected by an edge or not. For an undirected network, $A_{i}j = A_{j}i$. The abstraction of complex systems into networks has proven to be a powerful tool for understanding a number of phenomena spanning a wide array of disciplines. However, it is becoming increasingly clear that this abstract representation is not sufficient to fully understand the properties of systems where physicality is important (2–5). These "physical" networks correspond to systems with excluded volume interactions between the nodes and edges (i.e., they cannot overlap or occupy the same space), and therefore, the spatial distribution of their nodes and edges assumes critical importance. Examples of physical networks include the neural networks of the brain (6–8), vascular networks (9), the mycorrhizal networks connecting fungi and plants (10, 11), and networks of interacting molecules (12–16). For these systems, it is necessary to combine the abstract representation of a network with real-space information.

As a physical network is densified, the excluded volume interactions between the nodes and edges become much more pronounced. One pertinent question therefore is how does physicality influence the structure of a network as it is densified? The answer to this question is important also for phase change materials for advanced memory applications (17), the elastic response of mechanical metamaterials (18–20), and the two-liquid hypothesis for supercooled water (21–25). The latter refers to the idea, proposed in the early 1990s, that supercooled water can exist in two liquid phases separated by first-order liquid–liquid phase transition (LLPT) lines. This hypothesis has since been verified for several atomic, molecular, and colloidal systems (16, 25–28). The LLPT phenomenon is very often observed in systems of particles with limited valency and strong directional interactions (25), and so, these systems can be unambiguously represented as a network where nodes represent particles and edges connect bonded particles.

To investigate the interplay between accessible volume and the structure of physical networks we numerically study a model for DNA dendrimers (branched polymeric molecules), where each dendrimer is represented by a repulsive spherical core decorated with four attractive patches in a tetrahedral arrangement (29, 30). Depending on the temperature and pressure, the dendrimers can form three distinct network liquids of significantly different densities (separated by LLPTs) (31). Therefore, they represent an ideal model system for exploring how the density of a physical network affects its structure. We probe the geometry and topology of the dendrimer networks by focusing on ring motifs (a ring is a cyclic path in the network where the first and last nodes are the same). Our analyses show that the three network liquids not only differ in density but also in their topology:

Author affiliations: [a]Dipartimento di Fisica, Sapienza Universitá di Roma, Roma 00185, Italy; [b]School of Chemistry, University of Birmingham, Birmingham B15 2TT, United Kingdom; [c]Department of Physics, Wesleyan University, Middletown, CT 06459; and [d]International Institute for Sustainability with Knotted Chiral Meta Matter, Hiroshima University, Higashi-Hiroshima, Hiroshima 739-8526, Japan

Author contributions: A.N., F.W.S., D.C., and F.S. designed research; A.N. and F.W.S. performed research; A.N. analyzed data; and A.N., F.W.S., D.C., and F.S. wrote the paper.

The authors declare no competing interest.

This article is a PNAS Direct Submission.

[1]To whom correspondence may be addressed. Email: andreas.neophytou@uniroma1.it or francesco.sciortino@uniroma1.it.

This article contains supporting information online at https://www.pnas.org/lookup/suppl/doi:10.1073/pnas.2406890121/-/DCSupplemental.

At low pressures, an unentangled low-density liquid (LDL) forms; then, at intermediate pressures, an entangled high-density liquid (HDL) forms, and at high pressures, an entangled very high-density liquid (vHDL) forms. The topological distinction between the two entangled network liquids is revealed by probing their network of linked rings. In this "link-network" representation, nodes signify rings formed by the dendrimers, and edges are drawn between two rings that are linked. We show that the vHDL forms "rings of linked rings" of various size, while the HDL mostly forms branched chains of linked rings. Therefore, with increasing pressure, the dendrimers undergo a hierarchy of topological transitions signaled by step-growths in entanglement where, first rings form, then linked rings form, and finally rings (or cycles) of linked rings emerge.

Results and Discussion

Fig. 1*A* shows the equation of state for the dendrimer system as determined from isobaric-isothermal (NPT) Monte Carlo simulations for $N = 1{,}000$ dendrimers with arms of length L at the temperature $T^* = 0.085$ (see *Methods* for more details regarding the model). The equation of state shows three distinct liquid branches of differing densities: i) a LDL for pressures $P^* < 7$, ii) a HDL for $7 \le P^* \le 28$, and iii) a vHDL for $P^* \ge 28$. Fig. 1 *B–D* show snapshots of typical configurations from each of these liquid phases, where we have drawn cylinders between the centers of particles that are directly bonded to one another to generate a network representation of the liquids.

To associate spatial information with the connectivity of the network, we calculate the radial distribution function (RDF) $g(r)$—a measure for the probability of finding two particles at a spatial distance r—and decompose it into contributions derived from particles separated by D bonds: $g(r) = \sum_D g_D(r)$ (32). This decomposition allows us to assess whether particles close in space are separated by multiple bonds in the network. Fig. 1 *E–G* show $g_D(r)$ for values of D ranging from 1 to 6 for the LDL, HDL, and vHDL at pressures of $P^* = 2, 20,$ and 32, respectively. The positions for the peaks in g_1 and g_2 are similar in

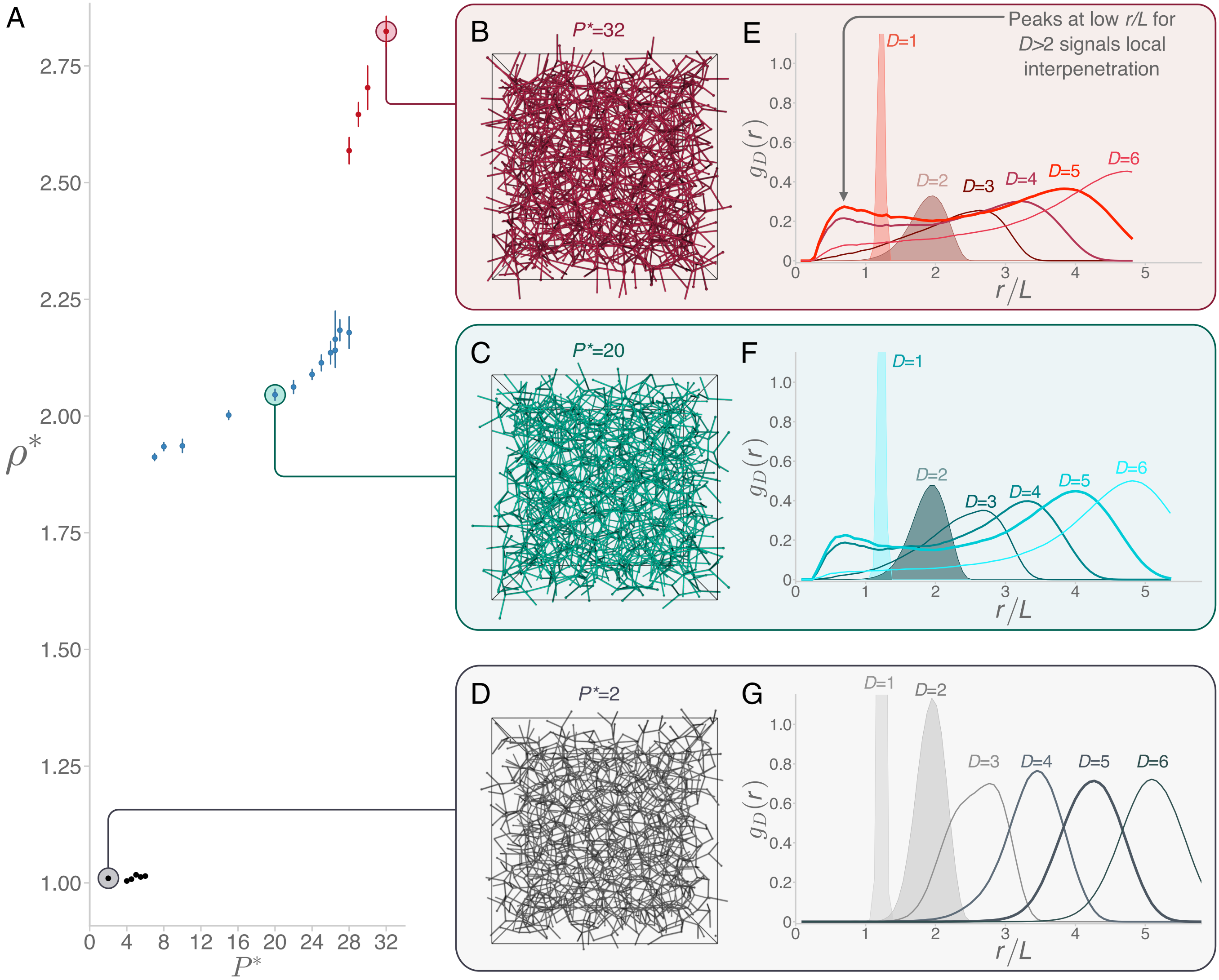

Fig. 1. Local interpenetration of networks across two liquid–liquid phase transitions for a coarse-grained model of tetrahedral DNA dendrimers. (*A*) Equation of state for the dendrimer model, highlighting the presence of two liquid–liquid phase transitions between three distinct liquids with different densities at a given temperature. (*B–D*) Snapshots of typical configurations from the three liquid phases in a network representation: (*B*) very high-density liquid, (*C*) high-density liquid, and (*D*) low-density liquid at pressures of $P^* = 32, 20, 2$, respectively. (*E* and *F*) Radial distribution functions for the model system, decomposed into the individual contributions derived from particles separated by D bonds, $g_D(r)$, for several D values, ranging from $D = 1$ to $D = 6$, at pressures of (*E*) $P^* = 32$, (*F*) $P^* = 20$, and (*G*) $P^* = 2$, respectively.

all three liquids, despite their differing densities, and are located at $r/L \approx 1$ and $r/L \approx 2$, respectively. In the LDL, the peaks for each $g_D(r)$ are well defined and there are no particles in the system lying at distances smaller than L, implying that there is no local interpenetration present in the LDL network (by local interpenetration we are referring to particles which are in close spatial proximity but do not share a bond). However, in the HDL and vHDL, the $g_D(r)$ distributions for $D > 2$ show a peak or shoulder at distances smaller than L, signaling the presence of local interpenetration. Interestingly, the local interpenetration is most pronounced for particles which are separated by $D = 4$ or $D = 5$ bonds. This observation reveals that a path along the network often returns close to its origin in real space after four or five bonds. As D increases further the peak at low r values gradually decreases in intensity until it practically disappears for $D \geq 8$.

To better understand how local interpenetration manifests we investigate the geometric and topological properties of the three liquids. We focus on three key structural motifs, which are all ring structures: i) coiled rings, ii) linked rings, and iii) knotted rings. These motifs are chosen since they all facilitate local interpenetration by bringing particles not directly bonded to one another into close spatial proximity, as evident in Fig. 2. A coiled ring is a cyclic path in the network whose geometry is greatly distorted from the expected planar-like geometry—much like how circular DNA undergoes supercoiling (33). Linked rings are two (or more) disjoint rings (i.e., rings that do not share any particles) which are entangled with one another in such a manner that they cannot be "unlinked" without at least one bond being broken. A knotted ring is a cyclic path in the network which adopts a self-entangled conformation that cannot be unentangled without a bond-breaking event. Additionally, in this third category, we include theta-curves which are two entangled rings that share at least two particles (see the lowest subpanel of Fig. 2).

To identify the presence of these structural motifs in the three liquid phases, we first enumerate all $\mathcal{N}_R$ shortest-path rings in each network (*Methods*) (34). Then, to quantify the degree of coiling and knotting we calculate the writhe

$$Wr_i = \frac{1}{4\pi} \oint_{C^i} \oint_{C^i} \frac{\boldsymbol{r}_i' - \boldsymbol{r}_i}{|\boldsymbol{r}_i' - \boldsymbol{r}_i|^3} \cdot (\mathrm{d}\boldsymbol{r}_i' \times \mathrm{d}\boldsymbol{r}_i), \qquad [1]$$

where $\boldsymbol{r}_i$ and $\boldsymbol{r}_i'$ represent two points along the perimeter of a cyclic path C^i and $\mathrm{d}\boldsymbol{r}_i$ and $\mathrm{d}\boldsymbol{r}_i'$ are two infinitesimal vectors along the perimeter of C^i with origins at $\boldsymbol{r}_i$ and $\boldsymbol{r}_i'$, respectively (16). In this work a cyclic path C is defined as the sequence of edges connecting the nodes of a shortest-path ring, or for a theta-curve it is the combined sequence of two fused rings excluding the edges connecting shared nodes (i.e., the backbone of the two fused rings; see Fig. 2). Eq. **1** measures the number of times a cyclic path C^i loops around itself (for instance, the writhe for the coiled ring and trefoil knot in Fig. 2 are $|Wr| \approx 1$ and $|Wr| \approx 3$, respectively). The total degree of knotting in the liquid networks is quantified using the network writhe (16),

$$\mathcal{W}_n = \sum_{i=1}^{\mathcal{N}_k} |Wr_i|, \qquad [2]$$

where we sum up the absolute writhes for the $\mathcal{N}_k$ knotted motifs (knotted rings and theta-curves) in the networks.

To identify links we calculate the linking number

$$Lk_{ij} = \frac{1}{4\pi} \oint_{R^i} \oint_{R^j} \frac{\boldsymbol{r}_j - \boldsymbol{r}_i}{|\boldsymbol{r}_j - \boldsymbol{r}_i|^3} \cdot (\mathrm{d}\boldsymbol{r}_j \times \mathrm{d}\boldsymbol{r}_i), \qquad [3]$$

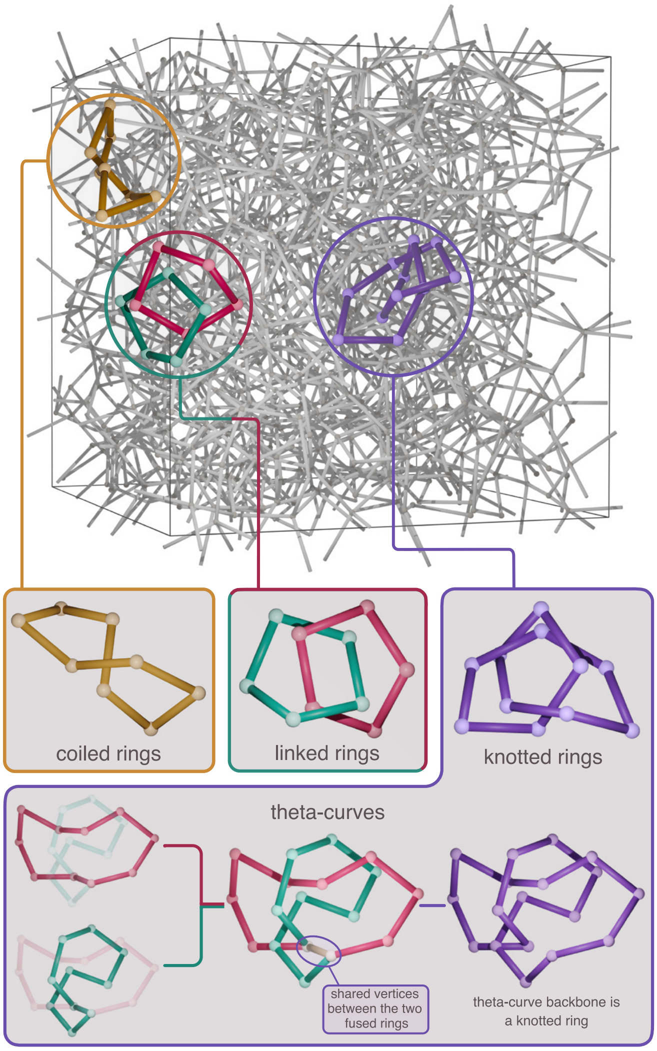

Fig. 2. Geometry and topology of rings in the very high-density liquid. Representative snapshot of the very high-density liquid at a pressure of $P^* = 32$, where three classes of structural motifs that drive local interpenetration in the network are highlighted: coiled rings (a ring whose geometry is distorted from a near-planar geometry), linked rings (two or more disjoint rings which are interlinked such that they cannot be separated without breaking a bond), and knotted rings (a self-entangled ring which cannot be unentangled without breaking a bond). Under the class of knotted rings, we also include theta-curves—two fused rings (i.e., rings that share at least two nodes) which are entangled—an example of which is shown in the lowest subpanel. The backbone of the theta-curve (which we show in purple on the right-hand side of the subpanel) is a knotted ring.

where Eq. **3** measures the number of times two disjoint rings, R^i and R^j, loop around one another (for instance, the link shown in Fig. 2 has a linking number of $|Lk| = 1$). Now $\boldsymbol{r}_i$ and $\boldsymbol{r}_j$ runs over the perimeter of two distinct rings R^i and R^j. Finally, we compute the total degree of linking in the liquid networks using the network linking number (3, 16)

$$\mathcal{L}_n = \sum_{i=0}^{\mathcal{N}_R} \sum_{i>j}^{\mathcal{N}_R} {}^{*} |Lk_{ij}|, \qquad [4]$$

where the * indicates that the sum only runs over pairs of disjoint rings. Note that we have taken the absolute values of Wr and Lk while computing the network writhe and linking number, thereby ignoring the sign which indicates their chirality, since our objective is to have a quantitative measure of the entanglement. Additionally, since the rings here are closed polygonal paths we compute the double line integrals in Eqs. **1** and **3** using expressions for polylines (*Methods*).

Geometric Changes in the Network Liquids. Fig. 3*A* shows the ring statistics as a function of pressure, where we have plotted the number of shortest-path rings ($\mathcal{N}_{R_l}$) of size $l \in [4-10]$ as a function of P^*. The plots show that as P^* increases the number of "small" rings ($l \leq 7$) decreases while the number of "large" rings ($l \geq 8$) increases. The number of rings shows clear discontinuous jumps concomitant with the change in density associated with each LLPT (Fig. 1*A*), confirming that an increase in density is associated to a change in the network connectivity.

We next probe how the geometry of the rings changes with ρ^* using the writhe. Fig. 3 *B*–*D* show the probability densities for the absolute writhe of the shortest-path rings in the LDL, HDL, and vHDL networks. The distributions show that as P^* increases (and therefore as ρ^* increases) larger rings find it much easier to adopt coiled geometries, while smaller rings remain planar-like. This is made clear by the progressive broadening of the distributions for $l > 6$, and by the *Insets* in Fig. 3 *B*–*D* where we show each ring with the largest absolute writhe for the given l and P^*. In particular, a substantial broadening appears with increasing P^* for the distributions of the 9- and 10-membered rings.

From this analysis we learn the following about the liquid networks: the average ring size, $\langle l \rangle$, and the average absolute writhe, $\langle |Wr| \rangle$, increases with P^*. However, $\langle |Wr| \rangle$ is still relatively small for all P^* considered ($\langle |Wr| \rangle < 0.2$) as signaled by the peaks of the distributions in Fig. 3 *B*–*D*. Therefore, while coiled rings (which have $|Wr| \gtrsim 1$) are more abundant in the HDL and vHDL networks as compared to the LDL, they are still a minority of the ring population. Although the formation of these coiled rings must contribute to the increased local interpenetration (and density) of the HDL and vHDL networks, we argue it is likely not the primary mechanism for densification. Interestingly, this means that the increase in pressure produces networks that are denser, and yet they contain larger rings which for the most part stay close to planar geometries ($|Wr| \approx 0$). Naively, one could expect that increasing the size of the rings in the network (without coiling) would decrease the density (due to the area of the ring pore increasing); instead, the opposite is true here. Hence, we reason that the formation of these larger rings must be accompanied by the formation of theta-curves or links.

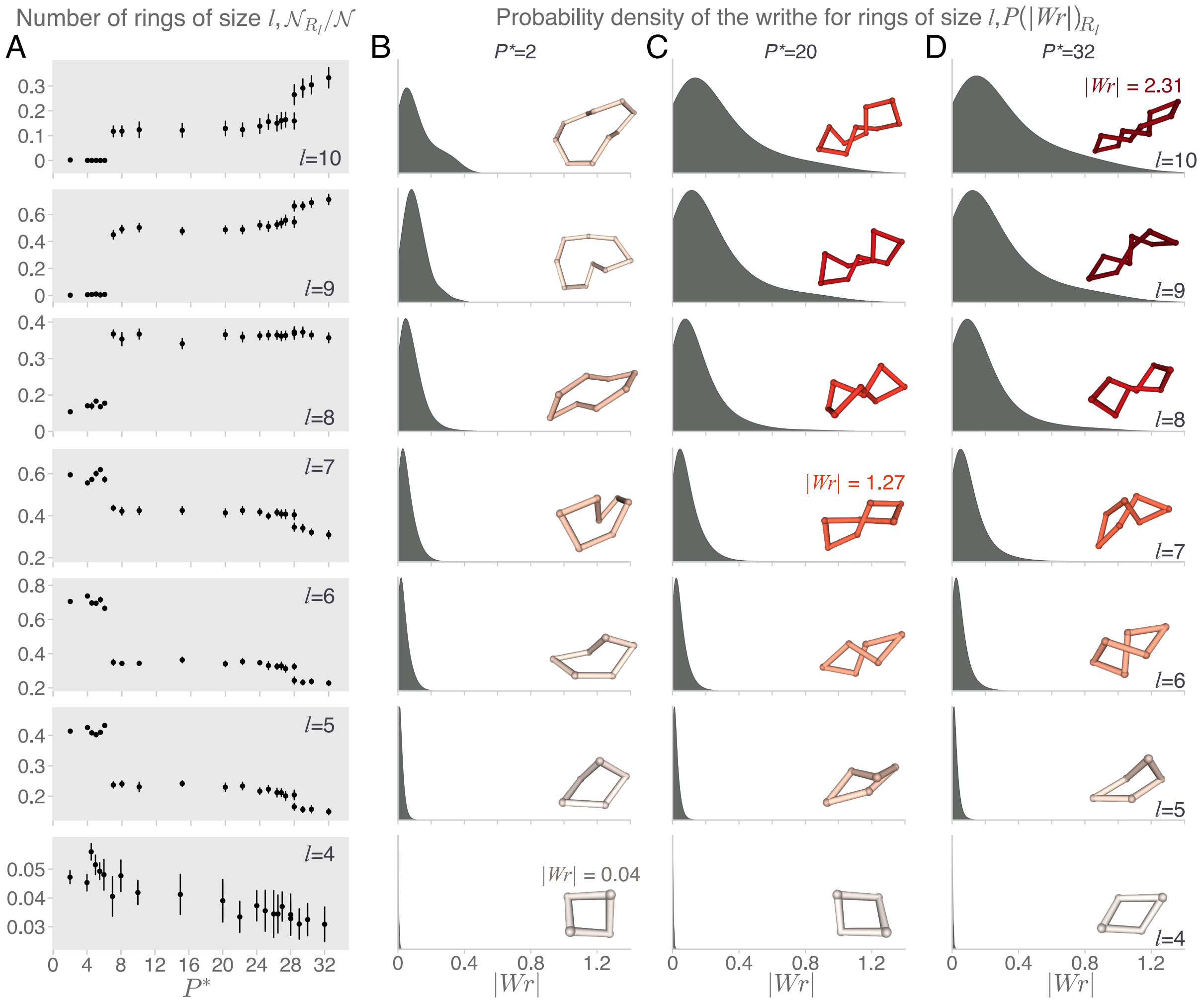

Fig. 3. Evolution of ring statistics and ring geometry across liquid–liquid phase transitions. (*A*) Dependence of the number of shortest-path rings ($\mathcal{N}_R$) for rings of different sizes (rings containing between 4 and 10 particles) normalized by the total number of particles ($\mathcal{N}$) as a function of pressure (P^*). (*B*–*D*) Probability density of the absolute writhe ($|Wr|$) for rings of different sizes for systems at pressures of (*B*) $P^* = 2$, (*C*) $P^* = 20$, and (*D*) $P^* = 32$. For each plot, the *Inset* shows the ring of the given size at the given pressure with the largest absolute writhe.

Topological Changes in the Network Liquids. Next, we probe the formation of links, knots, and theta-curves (the latter being fused rings that are entangled with one another; see Fig. 2). Fig. 4 *A* and *B* show the dependence of the average network writhe, $\mathcal{W}_n$, and network linking number, $\mathcal{L}_n$, (see Eqs. **2** and **4**, respectively), on P^*. The plots show that, as for the number of rings, there are two discontinuous jumps in both $\mathcal{W}_n$ and $\mathcal{L}_n$ concomitant with the jumps in density (Fig. 1*A*) across the successive LLPTs. Both $\mathcal{W}_n$ and $\mathcal{L}_n$ are zero in the LDL phase, showing that the LDL is unentangled. Given that $\mathcal{W}_n > 0$ and $\mathcal{L}_n > 0$ for both the HDL and vHDL phases, the LDL to HDL transition is from an unentangled to an entangled network, while the HDL to vHDL transition is between two entangled networks, with a significant growth in the degree of entanglement as the density increases.

Despite clearly signaling the LLPTs, only a small number of rings participate in a knotted motif. The total number of knotted motifs $\mathcal{N}_k$ is a small fraction of the total number of rings $\mathcal{N}_R$ (reaching a maximum value of only about 3% in the vHDL), whereas there are more links in the network than rings, meaning that there are many multiply linked rings. This is demonstrated in *SI Appendix*, Fig. S1, where we plot the knotting probability (equal to the total number of knotted motifs divided by the total number of rings: $\mathcal{P}_k = \mathcal{N}_k/\mathcal{N}_R$) as a function of pressure. Additionally, we find that $3.3\mathcal{P}_k \approx \mathcal{W}_n/\mathcal{N}_R$, highlighting that nearly all knotted motifs formed in the liquid networks correspond to trefoil knots adopting idealized conformations (16, 35).

To understand why $\mathcal{N}_k$ is so small as compared to $\mathcal{N}_R$, we show the probability density of the writhe limited to rings that are a part of at least one theta-curve, $P(|Wr|)_\theta$, in Fig. 4*C*. We find that two peaks appear at $|Wr| \approx 0$ and $|Wr| \approx 1$, suggesting that when theta-curves form it is frequently due to a planar and coiled ring becoming entangled (this is true for the theta-curve shown in Fig. 2). For comparison, Fig. 4*D* shows a similar probability density but now limited to rings that are a part of at least one link, $P(|Wr|)_{Lk}$. There is only a single peak in $P(|Wr|)_{Lk}$ at $|Wr| \approx 0$, highlighting that linked rings in the networks usually adopt a near-planar geometry. This suggests that local interpenetration is primarily driven by linking, with coiling and knotting playing a secondary role.

To further clarify the relationship between the formation of linked rings and the local interpenetration identified in Fig. 1 *E* and *F* (and the peaks in these figures), we compute the shortest bonded path (D_{Lk}) between each particle on any two linked rings i and j of size l_i and l_j (i.e., we compute the shortest bonded path between each of the $l_i \times l_j$ pairs of particles). Fig. 4*D* shows the probability density for D_{Lk} averaged over all pairs of linked rings in the vHDL. $P(D_{Lk})$ has a peak between $D_{Lk} = 4$ and $D_{Lk} = 5$, which is consistent with the RDFs shown in Fig. 1 *E* and *F* where local interpenetration is found to be maximized between particles separated by $D = 4$ or $D = 5$ bonds. Fig. 4*E* shows a pair of linked rings along with the example paths connecting their particles.

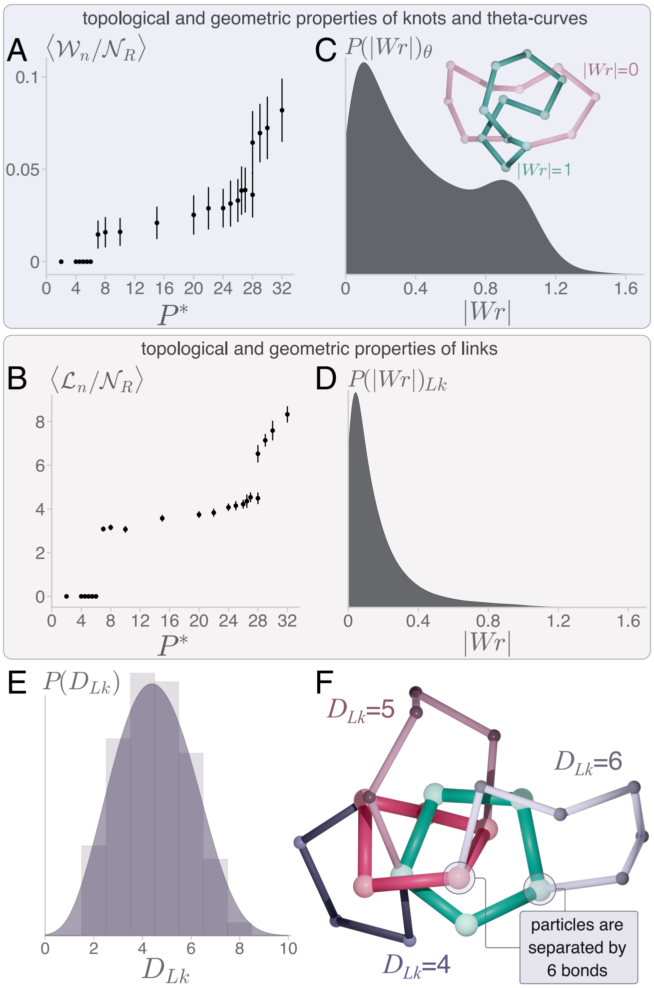

Fig. 4. Local interpenetration of network liquids driven by changes in ring topology. Dependence of the (*A*) network writhe ($\mathcal{W}_n$) and (*B*) network linking number ($\mathcal{L}_n$) normalized by the total number of shortest-path rings ($\mathcal{N}_R$) as a function of pressure (P^*) for the dendrimer system. The probability density for the absolute writhe ($|Wr|$) for rings that are a part of (*C*) at least one theta-curve or (*D*) one link at a pressure of $P^* = 32$. The *Inset* of panel (*C*) shows an example theta-curve highlighting that one of the rings is coiled and contributes to the peak in $P(|Wr|)_\theta$ centered at $|Wr| = 1$. (*E*) Probability density for the number of bonds (D_{Lk}) separating two particles that belong to two linked rings (note that the corresponding histogram is also shown). (*F*) Visualization of a pair of linked rings (shown with red and green bonds) and example paths consisting of 4, 5, and 6 bonds connecting pairs of particles on the two rings.

The distinction between the LDL and the HDL is clear: the LDL is unentangled and the HDL is entangled. A similar clear-cut distinction cannot be made for the HDL and vHDL since both are entangled (even if there is a quantitative difference in the degree of entanglement). A pertinent question is whether there is any qualitative difference in the nature of the entanglements formed in the two high-density liquid phases. To address this question, we construct a higher-order network representation of linked rings, transforming each shortest-path ring into a node and connecting two such nodes if the original rings are linked together. Fig. 5*A* shows a schematic illustration for the construction of such a "link-network." Each link-network is composed of $\mathcal{N}_R$ nodes and $\mathcal{L}_n$ edges. To avoid confusion we will refer to cyclic paths in these link-networks as cycles (as opposed to rings). Fig. 5 *B* and *C* show representative visualizations of link-networks for the HDL and vHDL phases, respectively, highlighting how highly connected both link-networks are in comparison to their parent networks. Note that the corresponding visualization of the link-network for the LDL would simply be a collection of nodes with no edges.

Often it is possible to characterize networks according to their degree distributions $p(k)$, where the degree k of a node is the number of edges connected to it. Each node in the link-network represents a ring of size l, therefore we computed the degree distributions for nodes with different l values separately. Fig. 5 *D* and *E* show the degree distributions $p(k_l)$ for the HDL and vHDL link-networks, respectively. The degree distributions for

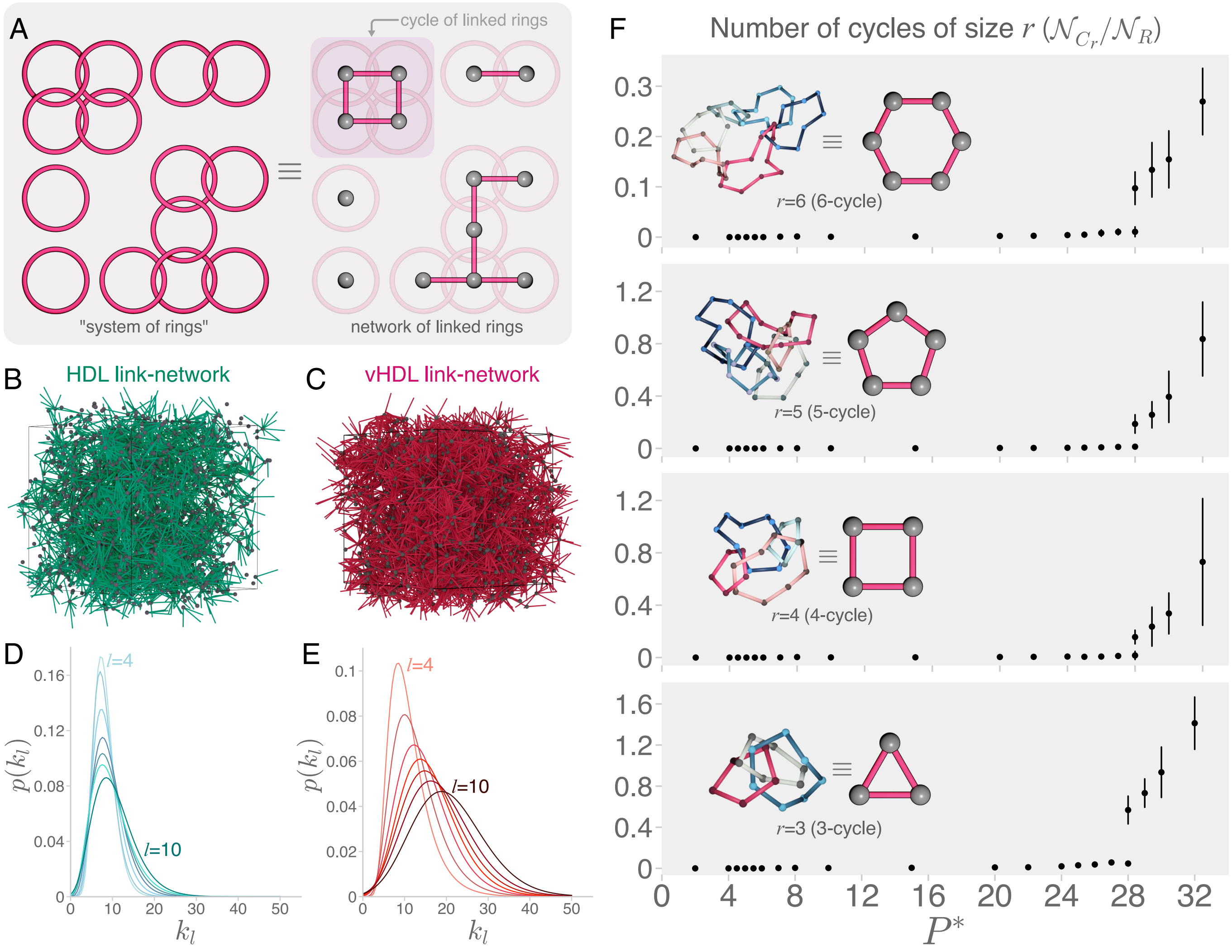

Fig. 5. Topological changes in the network of rings across the transition between high-density liquid and very high-density liquid. (*A*) Schematic showing a network representation for a system of rings—the "link-network"—where each node, shown as a gray solid sphere, stands for a ring and an edge, depicted as a pink cylinder, appears between two nodes if the corresponding rings are linked. Cyclic paths can form within this network of rings, as highlighted, and are referred to as cycles of rings. (*B* and *C*) Visualization of the link-network for the (*B*) high-density (HDL) and (*C*) very high-density liquid (vHDL) phases at pressures $P^* = 20$ and $P^* = 32$, respectively. (*D* and *E*) Degree distributions $p(k_l)$ for the (*D*) HDL and (*E*) vHDL link-networks at pressures $P^* = 20$ and $P^* = 32$, respectively. The distributions are generated by fitting to an inverse Gaussian function. (*F*) Evolution of the number of shortest-path cycles of size r ($\mathcal{N}_{C_r}$) in the link-network, normalized by the total number of rings ($\mathcal{N}_R$), as a function of P^* for $r = [3 \text{ to } 6]$. The *Insets* show representative illustrations for cycles size r found in the vHDL. Note that here r stands for the number of nodes in the shortest-path cycles of rings in the link-network, where the rings themselves may differ in their size l.

the link-networks of both the HDL and vHDL are well described by an inverse Gaussian distribution, indicating that they are both examples of random networks. However, the degree distributions do highlight a clear difference between the HDL and vHDL. The peaks in $p(k_l)$ of the HDL are practically insensitive to l, while for the vHDL we see that the peaks clearly shift to larger values with increasing l. This means that the ability for larger rings to form more links (due to the larger area of their pore allowing for more linking) manifests in the vHDL but not the HDL. Additionally, we notice that at high pressures there are some highly connected nodes ($k \approx 70$) in the link-network of the vHDL.

We next investigate the presence of shortest-path cycles within the link-networks, excluding the cycles that contain fused rings. Fig. 5*F* shows the evolution of the average number of cycles ($\mathcal{N}_{C_r}$) of size $r \in [3 \text{ to } 6]$ in the link-networks as a function of pressure. Fig. 5*F* reveals an important topological distinction between the HDL and vHDL networks: The HDL link-networks contain very few cycles (they are tree-like networks) while the vHDL link-networks contain a large number of cycles. The *Insets* of Fig. 5*F* show illustrative examples of cycles found in the vHDL networks. These results indicate that the HDL–vHDL transition is between two entangled networks that differ in the connectivity of their entanglements.

Summary and Outlook

In summary, an increase in the density of a physical network composed of nodes with fixed valency requires an increase in their topological complexity. We demonstrate this by studying a coarse-grained model for nanoparticles functionalized with four single strands of DNA (dendrimers) which is known to form three distinct network liquids—the LDL, HDL, and vHDL—depending upon the pressure. We find that as the density increases across the LLPTs, the average ring size $\langle l \rangle$ gradually increases in the three networks, with $\langle l_{\mathrm{LDL}} \rangle \approx 6$, $\langle l_{\mathrm{HDL}} \rangle \approx 7$ to 8 and $\langle l_{\mathrm{vHDL}} \rangle \approx 9$, indicating that larger rings facilitate the formation of higher-density configurations. Densification is made possible by the associated increase in the linking capacity, with the networks becoming progressively more entangled. As a result, the LDL is an unentangled network liquid, and the HDL and vHDL are both entangled liquids. Remarkably, while the HDL and vHDL are both examples of entangled network liquids, they have distinct topological properties. We reveal this difference by investigating the connectivity of the entanglements in the two liquids. In our representation, each ring formed by the dendrimers corresponds to a "meta-particle" that can become "bonded" to other meta-particles through linking [in analogy to the mechanical bonds in mechanically interlocked molecules, such as rotaxanes and catenanes, formed via supramolecular chemistry(36, 37)]. This allows us to show that the cascade of network phases of increasing density follows a hierarchy of topological transitions via a staged self-assembly process involving i) the formation of rings; ii) the formation of linked rings; iii) the formation of rings of linked rings.

More concisely, a physical network embedded in three-dimensional space (where interactions between the nodes determine its layout) must increase its topological complexity to become denser without changing its local connectivity.

It is worth noting that the network linking number has some limitations as an order parameter for capturing the presence of topological linking in physical networks. Most notably, for some higher-order links $Lk = 0$. For example, this is the case for the Whitehead link (38). In the future, it may be of interest to apply more powerful invariants, such as the twisted Alexander polynomial (39) or the Jones polynomial (40), to the topological analysis of physical networks.

Here we have focused on understanding how changes in density affect the topology of a network liquid. However, it is also of interest to probe how these topological changes alter dynamical and mechanical properties. In *SI Appendix*, Fig. S2 *A* and *B*, we show the mean squared displacement (MSD) and bond autocorrelation function for the LDL, HDL, and vHDL networks at pressures of $P^* = 2, 20,$ and 32, respectively. Interestingly, we find that the dynamics speed up considerably as the topological complexity of the networks increases [a similar effect occurs in water (16, 41)]. This dynamical speed-up can also be observed by monitoring the lifetime of rings in the networks (as shown in Movie S1) or the lifetime of linked rings (as shown in Movie S2). This is in contrast to polymer melts (42, 43) or active melts of ring polymers (44) where the formation of topological entanglements results in a slowing of the dynamics or even vitrification. In the future, it will therefore be of interest to understand the mechanism by which topological entanglement in network liquids facilitates faster dynamics.

Methods

Tetrahedral Dendrimer Model. The coarse-grained model used in this work represents macromolecules composed of a repulsive core decorated by four short single-stranded DNA (ssDNA) where two particles i and j interact via the pairwise potential (45)

$$V_{ij}(r_{ij}, \Omega_i, \Omega_j, T^*) = V_{\mathrm{core}}(r_{ij}) + \sum_{\alpha,\beta=1}^{4} p_{\alpha\beta}(T^*) V_{\mathrm{patch}}(r_{ij}, L, \theta_\alpha, \theta_\beta), \quad [5]$$

where $r_{ij} = |\mathbf{r}_{ij}|$ is the distance between the centers of the two particles, Ω_i and Ω_j describe the orientations of the two particles, and T^* is the reduced temperature. The pair potential has two components: i) a very short-ranged repulsive component V_{core} which is isotropic and depends only on r_{ij}; ii) an attractive component V_{patch} that captures the lock-and-key nature of base-pairing between the ssDNA arms of length L, and so depends not only on the distance between the particles but also their orientation and the temperature (which enters via the bonding probability function $p_{\alpha\beta}$), where θ_α is the angle between the unit vector describing the direction of patch α on particle i and $\hat{\mathbf{r}}_{ij}$ and likewise θ_β is the angle between patch β on particle j and $\hat{\mathbf{r}}_{ij}$. Importantly, $p_{\alpha\beta}$ not only captures the temperature dependence of the binding between two ssDNA arms but also the limited valency (i.e., $p_{\alpha\beta} = 0$ if patch α or patch β are already bonded to another patch). The functional forms of V_{core}, V_{patch}, and $p_{\alpha\beta}$ were originally determined numerically by simulating a system where the ssDNA arms are explicitly considered (45). The distribution of arm orientations over which a bond may form is parameterized by a Gaussian function, and the variance σ^2 of that Gaussian has subsequently been treated as an adjustable parameter to alter the bond orientational flexibility, which in turn alters the relative stability of amorphous and crystalline phases (46). Here we use $\sigma^2 = 1/16$. The dendrimer arms represent 8-base ssDNA strands. Using this strand length, the potential vanishes for separations larger than 12.5 (in units of the diameter of a single base). Energy is measured in units of the attractive strength between two base pairs in the original explicit model denoted by the symbol ε (29).

Monte Carlo Simulations. We performed a series of Monte Carlo simulations in the *NPT* ensemble for $N = 1{,}000$ dendrimer particles at a reduced temperature of $T^* = k_{\mathrm{B}}T/\varepsilon = 0.085$ (where k_{B} is the Boltzmann constant which is taken to be equal to one in this work). Simulations were run at reduced pressures in the range $P^* = 10^5 Pd^3/\varepsilon \in [2 \text{ to } 32]$ (where d is the most probable separation between the centers of two bonded dendrimers which corresponds to the value of r_{ij}, where V_{ij} is minimized) in order to determine the equation of state where the reduced density is given by $\rho^* = Nd^3/V$ (where V is the volume). Each simulation was run for a minimum of 2×10^8 Monte Carlo cycles, where each cycle consists of either a molecular displacement and reorientation (with probability $(N-1)/N$) or a volume change (with probability $1/N$). At least 100 configurations, equally spaced in time, along the trajectory were saved for computing the geometric and topological properties of the networks. In the simulations, each particle is treated as a rigid body whose orientational degrees of freedom were represented by quaternions.

Ring Enumeration and Topological Analysis. To compute the geometric and topological properties of the network liquids, we first extracted the adjacency matrix $\mathcal{A}_{ij}$ of each configuration, where two particles i and j were considered connected by an edge if they shared a patch–patch interaction (which was determined using Eq. **5**). Once the adjacency matrix of a network was computed we identified shortest-path rings. Starting from each node i of the network we found the shortest path connecting any two of its bonded neighbors l and m (which does not include i), then adding node i to this path produces a shortest-path ring. This was then repeated for all pairs of bonded neighbors l and m. If there were multiple "shortest" paths of the same length connecting l and m, then all resulting rings were added to the set of shortest-path rings.

The rings formed by the dendrimer particles are composed of nodes connected by straight line segments, therefore they represent closed polygonal paths. This allows us to compute the writhe of a ring as (33)

$$Wr_i(\mathrm{R}_i) = \frac{1}{2\pi} \sum_{k \neq l} \omega_{kl}, \quad [6]$$

where ω_{kl} is the contribution to the writhe from the segments k and l on ring i defined as (33)

$$\begin{aligned} \omega_{kl} = \mathrm{sgn}\big\{[(\boldsymbol{r}_{l+1} - \boldsymbol{r}_l) \times (\boldsymbol{r}_{k+1} - \boldsymbol{r}_k)] \cdot \mathbf{a}\big\} \cdot \\ \big(\sin^{-1}(\boldsymbol{n}_1 \cdot \boldsymbol{n}_2) + \sin^{-1}(\boldsymbol{n}_2 \cdot \boldsymbol{n}_3) \\ + \sin^{-1}(\boldsymbol{n}_3 \cdot \boldsymbol{n}_4) + \sin^{-1}(\boldsymbol{n}_4 \cdot \boldsymbol{n}_1)\big), \end{aligned} \quad [7]$$

where sgn(·) is the sign function and

$$\boldsymbol{n}_1 = \frac{\mathbf{a}\times\mathbf{d}}{|\mathbf{a}\times\mathbf{d}|},\quad \boldsymbol{n}_2 = \frac{\mathbf{d}\times\mathbf{c}}{|\mathbf{d}\times\mathbf{c}|},$$
$$\boldsymbol{n}_3 = \frac{\mathbf{c}\times\mathbf{b}}{|\mathbf{c}\times\mathbf{b}|},\quad \boldsymbol{n}_4 = \frac{\mathbf{b}\times\mathbf{a}}{|\mathbf{b}\times\mathbf{a}|}, \qquad [8]$$

where $\mathbf{a} = \boldsymbol{r}_l - \boldsymbol{r}_k$, $\mathbf{b} = \boldsymbol{r}_l - \boldsymbol{r}_{k+1}$, $\mathbf{c} = \boldsymbol{r}_{l+1} - \boldsymbol{r}_{k+1}$, and $\mathbf{d} = \boldsymbol{r}_{l+1} - \boldsymbol{r}_k$. To identify whether a ring (or the backbone for a pair of fused rings) is knotted, we used the python package pyknotid (47).

The linking number can similarly be computed using

$$Lk_{ij}(\mathrm{R}_i, \mathrm{R}_j) = \frac{1}{4\pi}\sum_{kl}\lambda_{kl}, \qquad [9]$$

where λ_{kl} is the contribution to the Lk_{ij} from a pair of line segments k and l belonging to rings i and j, respectively, and

$$\lambda_{kl} = \operatorname{atan}\left(\frac{\mathbf{a}\cdot(\mathbf{b}\times\mathbf{c})}{|\mathbf{a}||\mathbf{b}||\mathbf{c}| + (\mathbf{a}\cdot\mathbf{b})|\mathbf{c}| + (\mathbf{c}\cdot\mathbf{a})|\mathbf{b}| + (\mathbf{b}\cdot\mathbf{c})|\mathbf{a}|}\right)$$
$$+ \operatorname{atan}\left(\frac{\mathbf{c}\cdot(\mathbf{d}\times\mathbf{a})}{|\mathbf{c}||\mathbf{d}||\mathbf{a}| + (\mathbf{c}\cdot\mathbf{d})|\mathbf{a}| + (\mathbf{a}\cdot\mathbf{c})|\mathbf{d}| + (\mathbf{d}\cdot\mathbf{a})|\mathbf{c}|}\right), \qquad [10]$$

where **a**, **b**, **c**, and **d** are defined as before (48).

Dynamical Properties. To probe the dynamical properties of the network liquids we compute the MSD and bond autocorrelation function (C_b). The bond autocorrelation function represents the fraction of bonds which are still present in the system following t Monte Carlo cycles (i.e., we are taking a single Monte Carlo cycle to be the unit of time), independent of whether any bond breaking events occurred during the interim. We define it as

$$C_\mathrm{b}(t) = \left\langle \frac{\sum_i\sum_j \mathcal{A}_{ij}(t')\mathcal{A}_{ij}(t'+t)}{\sum_i\sum_j \mathcal{A}_{ij}(t')} \right\rangle, \qquad [11]$$

where $\mathcal{A}(t')$ is the adjacency matrix at "time" t' and $\mathcal{A}_{ij} = 1$ or $\mathcal{A}_{ij} = 0$ if particles i and j are bonded or not bonded to one another, respectively. Additionally, we take the average over all possible time origins t'.

Data, Materials, and Software Availability. All data code can be found at (49).

ACKNOWLEDGMENTS. We thank I. Bonamassa for helpful discussions. We also gratefully acknowledge support from the Royal Society via International Exchanges Award IES\R3\183166. A.N. and D.C. thank the Institute of Advanced Studies, the BlueBEAR high-performance computing service of the University of Birmingham, and the Turing Scheme. F.S. acknowledges support from MIUR-PRIN 2022JWAF7Y, Cineca Italian Super Computing Resource Allocation initiative, and X-Calculus (ICSC)-Centro Nazionale di Ricerca in High Performance Computing, Big Data and Quantum Computing, funded by the European Union "NextGenerationEU."

1. M. Newman, *Networks* (Oxford University Press, 2018).
2. N. Dehmamy, S. Milanlouei, A. L. Barabási, A structural transition in physical networks. *Nature* **563**, 676–680 (2018).
3. Y. Liu, N. Dehmamy, A. L. Barabási, Isotopy and energy of physical networks. *Nat. Phys.* **17**, 216–222 (2021).
4. M. Pósfai *et al.*, Impact of physicality on network structure. *Nat. Phys.* **20**, 142–149 (2024).
5. I. Bonamassa *et al.*, Bundling by volume exclusion in non-equilibrium spaghetti. arXiv [Preprint] (2024). https://doi.org/10.48550/arXiv.2401.02579 (Accessed 10 January 2024).
6. T. McKenna, T. McMullen, M. Shlesinger, The brain as a dynamic physical system. *Neuroscience* **60**, 587–605 (1994).
7. O. Sporns, Network analysis, complexity, and brain function. *Complexity* **8**, 56–60 (2002).
8. L. Pessoa, Understanding brain networks and brain organization. *Phys. Life Rev.* **11**, 400–435 (2014).
9. C. O'Connor, E. Brady, Y. Zheng, E. Moore, K. R. Stevens, Engineering the multiscale complexity of vascular networks. *Nat. Rev. Mater.* **7**, 702–716 (2022).
10. E. K. Barto, J. D. Weidenhamer, D. Cipollini, M. C. Rillig, Fungal superhighways: Do common mycorrhizal networks enhance below ground communication? *Trends Plant Sci.* **17**, 633–637 (2012).
11. S. W. Simard *et al.*, Mycorrhizal networks: Mechanisms, ecology and modelling. *Fungal Biol. Rev.* **26**, 39–60 (2012).
12. W. H. Zachariasen, The atomic arrangement in glass. *J. Am. Chem. Soc.* **54**, 3841–3851 (1932).
13. R. Bell, P. Dean, The structure of vitreous silica: Validity of the random network theory. *Philos. Mag.* **25**, 1381–1398 (1972).
14. A. Wright, M. Thorpe, Eighty years of random networks. *Phys. Status Solidi B Basic Res.* **250**, 931–936 (2013).
15. Z. H. Jiang, Q. Y. Zhang, The structure of glass: A phase equilibrium diagram approach. *Prog. Mater. Sci.* **61**, 144–215 (2014).
16. A. Neophytou, D. Chakrabarti, F. Sciortino, Topological nature of the liquid-liquid phase transition in tetrahedral liquids. *Nat. Phys.* **18**, 1248–1253 (2022).
17. P. Zalden *et al.*, Femtosecond X-ray diffraction reveals a liquid-liquid phase transition in phase-change materials. *Science* **364**, 1062–1067 (2019).
18. A. A. Zadpoor, Mechanical meta-materials. *Mater. Horiz.* **3**, 371–381 (2016).
19. K. Bertoldi, V. Vitelli, J. Christensen, M. Van Hecke, Flexible mechanical metamaterials. *Nat. Rev. Mater.* **2**, 1–11 (2017).
20. M. Kadic, G. W. Milton, M. van Hecke, M. Wegener, 3D metamaterials. *Nat. Rev. Phys.* **1**, 198–210 (2019).
21. P. H. Poole, F. Sciortino, U. Essmann, H. E. Stanley, Phase behaviour of metastable water. *Nature* **360**, 324–328 (1992).
22. J. C. Palmer *et al.*, Metastable liquid-liquid transition in a molecular model of water. *Nature* **510**, 385–388 (2014).
23. P. G. Debenedetti, F. Sciortino, G. H. Zerze, Second critical point in two realistic models of water. *Science* **369**, 289–292 (2020).
24. K. H. Kim *et al.*, Experimental observation of the liquid-liquid transition in bulk supercooled water under pressure. *Science* **370**, 978–982 (2020).
25. J. Russo, F. Leoni, F. Martelli, F. Sciortino, The physics of empty liquids: From patchy particles to water. *Rep. Progr. Phys.* **85**, 016601 (2022).
26. Y. Katayama *et al.*, A first-order liquid-liquid phase transition in phosphorus. *Nature* **403**, 170–173 (2000).
27. S. Sastry, C. Austen Angell, Liquid-liquid phase transition in supercooled silicon. *Nat. Mater.* **2**, 739–743 (2003).
28. F. Smallenburg, L. Filion, F. Sciortino, Erasing no-man's land by thermodynamically stabilizing the liquid-liquid transition in tetrahedral particles. *Nat. Phys.* **10**, 653–657 (2014).
29. F. W. Starr, F. Sciortino, Model for assembly and gelation of four-armed DNA dendrimers. *J. Phys. Condens. Matter* **18**, L347 (2006).
30. J. Largo, F. W. Starr, F. Sciortino, Self-assembling DNA dendrimers: A numerical study. *Langmuir* **23**, 5896–5905 (2007).
31. C. W. Hsu, J. Largo, F. Sciortino, F. W. Starr, Hierarchies of networked phases induced by multiple liquid-liquid critical points. *Proc. Natl. Acad. Sci. U.S.A.* **105**, 13711–13715 (2008).
32. R. Foffi, J. Russo, F. Sciortino, Structural and topological changes across the liquid-liquid transition in water. *J. Chem. Phys.* **154**, 184506 (2021).
33. K. Klenin, J. Langowski, Computation of writhe in modeling of supercoiled DNA. *Biopolym. Orig. Res. Biomol.* **54**, 307–317 (2000).
34. S. Le Roux, P. Jund, Ring statistics analysis of topological networks: New approach and application to amorphous GeS2 and SiO2 systems. *Comput. Mater. Sci.* **49**, 70–83 (2010).
35. V. Katritch *et al.*, Geometry and physics of knots. *Nature* **384**, 142–145 (1996).
36. J. P. Sauvage, C. Dietrich-Buchecker, *Molecular Catenanes, Rotaxanes and Knots: A Journey Through the World of Molecular Topology* (John Wiley & Sons, 2008).
37. J. F. Stoddart, The chemistry of the mechanical bond. *Chem. Soc. Rev.* **38**, 1802–1820 (2009).
38. D. Rolfsen, *Knots and Links* (American Mathematical Soc., 2003), vol. No. 346.
39. S. Vidussi, *Twisted Alexander Polynomials in Encyclopedia of Knot Theory* (Chapman and Hall/CRC, 2021), pp. 631–636.
40. V. F. R. Jones, Hecke Algebra Representations of Braid Groups and Link Polynomials. *Ann. Math.* **126**, 335–388 (1987).
41. L. P. Singh, B. Issenmann, F. Caupin, Pressure dependence of viscosity in supercooled water and a unified approach for thermodynamic and dynamic anomalies of water. *Proc. Natl. Acad. Sci. U.S.A.* **114**, 4312–4317 (2017).
42. R. S. Porter, J. F. Johnson, The entanglement concept in polymer systems. *Chem. Rev.* **66**, 1–27 (1966).
43. D. C. Kong *et al.*, Control of polymer properties by entanglement: A review. *Macromol. Mater. Eng.* **306**, 2100536 (2021).
44. C. Micheletti, I. Chubak, E. Orlandini, J. Smrek, Topology-based detection and tracking of deadlocks reveal aging of active ring melts. *ACS Macro Lett.* **13**, 124–129 (2024).
45. J. Largo, P. Tartaglia, F. Sciortino, Effective nonadditive pair potential for lock-and-key interacting particles: The role of the limited valence. *Phys. Rev. E* **76**, 011402 (2007).
46. F. W. Starr, F. Sciortino, "Crystal-clear" liquid-liquid transition in a tetrahedral fluid. *Soft Matter* **10**, 9413–9422 (2014).
47. A. J. Taylor, Other SPOCK contributors, pyknotid knot identification toolkit (2017). https://github.com/575SPOCKnots/pyknotid. Accessed 4 September 2021.
48. A. Qu, D. L. James, Fast linking numbers for topology verification of loopy structures. *ACM Trans. Graph.* **40**, 106 (2021).
49. A. Neophytou, F. W. Starr, D. Chakrabarti, F. Sciortino, Research data supporting the publication "Hierarchy of Topological Transitions in a Network Liquid". Zenodo. https://doi.org/10.5281/zenodo.12720307. Deposited 5 August 2024.